Computer Methods and Programs in Biomedicine 238 (2023) 107600

Contents lists available at ScienceDirect

Computer Methods and Programs in Biomedicine

journal homepage: www.elsevier.com/locate/cmpb

Effect of pulmonary regurgitation on cardiac functions based on a human bi-ventricle model

Xueqing Yin[a], Yingjie Wang[a,*]

School of Mathematics and Statistics, University of Glasgow, Glasgow, United Kingdom

ARTICLE INFO

Article history:
Received 23 December 2022
Revised 27 April 2023
Accepted 13 May 2023

Keywords:
Biventricular function
Computational heart modelling
Finite element method
Pulmonary regurgitation
3D Realistic simulation
Right ventricular dilation

ABSTRACT

Background and objective: Assessing the severity of pulmonary regurgitation (PR) and identifying optimal clinically relevant indicators for its treatment is crucial, yet standards for quantifying PR remain unclear in clinical practice. Computational modelling of the heart is in the process of providing valuable insights and information for cardiovascular physiology research. However, the advancements of finite element computational models have not been widely applied to simulate cardiac outputs in patients with PR. Furthermore, a computational model that incorporates both the left ventricle (LV) and right ventricle (RV) can be valuable in assessing the relationship between left and right ventricular morphometry and septal motion in PR patients. To enhance our understanding of the effect of PR on cardiac functions and mechanical behaviour, we developed a human bi-ventricle model to simulate five cases with varying degrees of PR severity. Methods: This bi-ventricle model was built using a patient-specific geometry and a widely used myofibre architecture. The myocardial material properties were described by a hyperelastic passive constitutive law and a modified time-varying elastance active tension model. To simulate realistic cardiac functions and the dysfunction of the pulmonary valve in PR disease cases, open-loop lumped parameter models representing systemic and pulmonary circulatory systems were designed. Results: In the baseline case, pressures in the aorta and main pulmonary artery and ejection fractions of both the LV and RV were within normal physiological ranges reported in the literature. The end-diastolic volume (EDV) of the RV under varying degrees of PR was comparable to the reported cardiac magnetic resonance imaging data. Moreover, RV dilation and interventricular septum motion from the baseline to the PR cases were clearly observed through the long-axis and short-axis views of the bi-ventricle geometry. The RV EDV in the severe PR case increased by 50.3% compared to the baseline case, while the LV EDV decreased by 18.1%. The motion of the interventricular septum was consistent with the literature. Furthermore, ejection fractions of both the LV and RV decreased as PR became severe, with LV ejection fraction decreasing from 60.5% at baseline to 56.3% in the severe case and RV ejection fraction decreasing from 51.8% to 46.8%. Additionally, the average myofibre stress of the RV wall at end-diastole significantly increased due to PR, from 2.7±12.1 kPa at baseline to 10.9±26.5 kPa in the severe case. The average myofibre stress of the LV wall at end-diastole increased from 3.7±18.1 kPa to 4.3±20.3 kPa. Conclusions: This study established a foundation for the computational modelling of PR. The simulated results showed that severe PR leads to reduced cardiac outputs in both the LV and RV, clearly observable septum motion, and a significant increase in the average myofibre stress in the RV wall. These findings demonstrate the potential of the model for further exploration of PR.

© 2023 The Author(s). Published by Elsevier B.V.
This is an open access article under the CC BY-NC-ND license
(http://creativecommons.org/licenses/by-nc-nd/4.0/)

1. Introduction

Pulmonary regurgitation (PR) is a medical condition characterized by dysfunction of the pulmonary valve, leading to a backflow of blood into the right ventricle (RV) during diastole. A slight amount of PR was reported in 40–78% of individuals with normal pulmonary valves [1]. Mild-to-moderate PR is commonly observed in patients with pulmonary hypertension [2–4], while severe PR is a frequent complication in patients who have undergone repaired pulmonary valve procedures [5,6], particularly in cases of tetralogy of Fallot (TOF), which is a congenital heart defect occurring in some infants [7–9].

* Corresponding author.
E-mail address: y.wang.18@research.gla.ac.uk (Y. Wang).

https://doi.org/10.1016/j.cmpb.2023.107600
0169-2607/© 2023 The Author(s). Published by Elsevier B.V. This is an open access article under the CC BY-NC-ND license
(http://creativecommons.org/licenses/by-nc-nd/4.0/)

Severe PR can result in significant RV overload, bi-ventricle dysfunction, arrhythmias, and associated morbidity and mortality [10–12]. Therefore, evaluating the severity of PR is crucial for clinical decision-making and treatment planning. Currently, the two primary techniques for assessing PR are cardiac magnetic resonance (CMR) imaging and Doppler echocardiography, as they are capable of quantifying volumes of ventricles and flow [1,11,13,14]. Nevertheless, establishing standardized quantification measures for PR remains a challenge, and limitations and technical difficulties in imaging techniques continue to hinder accurate measurement and assessment of the impact of PR on cardiac functions [1,10,14–17].

Recent advancements in continuum mechanics, finite element (FE) method, high-performance computing, and clinical imaging techniques have enabled the development of computational models for accurately simulating and predicting the mechanical behaviours of the heart [18–24]. For instance, Wang et al. [20] created a FE model of the human left ventricle (LV) from CMR imaging data and incorporated a passive material model proposed by Holzapfel and Ogden [25] with a rule-based myofibre structure. Baillargeon et al. [21] developed the Living Heart Project, which simulated the behaviour of a human heart with all four chambers in a whole cardiac cycle. Their model included an active stress component during systole, added to the total Cauchy stress via a phenomenological representation of active contraction [18,26–28]. Additionally, they adopted a lumped parameter system to provide a natural coupling of pressures between the four chambers, and their simulated long-axis shortening and pressure-volume loops were consistent with clinical observations. Moreover, Sack et al. [22] constructed and validated subject-specific biventricular FE swine heart models in healthy and diseased states. They reported reference stress and strain values at multiple time points in one cardiac cycle, and their simulated stroke volume, ejection fraction, and strains agreed well with experimental data. Their computational model is widely regarded as one of the most sophisticated computational models of the heart. Guan et al. [24] used a similar FE computational model of a bi-ventricle porcine heart to demonstrate that sheet-normal active contraction enhanced ventricular contraction. They further investigated the effects of myofibre structure, including fibre rotation angle and dispersion, on cardiac passive and active responses [29,30]. Wisneski et al. [31] recently utilised the advanced four-chamber human heart model developed by Baillargeon et al. [21] to investigate the impact of aortic stenosis on myofibre stress. The degree of aortic stenosis was achieved by adjusting the resistance of the aortic valve. Additionally, they developed patient-specific LV models to investigate the effect of low-flow and low-gradient aortic stenosis on LV biomechanics [32], and observed globally reduced LV stress compared to stress in an idealized LV geometry. For further reading on advancements in computational heart modelling, comprehensive reviews can be found in [23,33–35].

Despite the advancements in FE computational models, they have not been widely applied to simulate cardiac motion and functions in patients with PR. Few computational models have been developed to simulate cardiac stress in PR patients and evaluate outcomes of TOF. For example, Tang et al. [36] introduced an RV/LV/Patch model to simulate cardiac stress and evaluate the effect of patch materials on RV functions. Later, Tang et al. [37] adapted their model to incorporate different zero-load diastole and systole geometries to reflect zero-stress sarcomere length changes in active contraction, providing more accurate cardiac stress calculations. More recently, Tang et al. [38] employed their model to study the mechanical stress and strain characteristics between PR patients after TOF repair and healthy individuals, suggesting that cardiac stress could be used as a potential indicator to evaluate TOF outcomes. Gusseva et al. [39] used a reduced-dimensional RV model with simplified spherical geometry to predict ventricular mechanics after TOF. These studies highlight the potential of computational modelling in PR studies, yet additional improvements are required to obtain more precise simulation and prediction of the complex three-dimensional (3D) cardiac motion during a complete cardiac cycle. Specifically, the utilisation of up-to-date constitutive laws, active tension models, myofibre structures, and dynamic responses is necessary.

Furthermore, the LV and RV are interdependent structures that share a common wall called the interventricular septum and are situated within the pericardium. A computational model that takes into account both the LV and RV can be valuable in assessing the interaction between the LV and RV pressures and volumes, as well as septal motion in PR conditions. Méndez et al. [40] demonstrated the usefulness of assessing septal wall motion from CMR imaging in evaluating hemodynamic status in patients with congenital and acquired heart disease in routine clinical practice. They concluded that abnormal septal motion warrants an additional emphasis on confirming and determining the severity of right-sided pressure and volume overload. Naeije and Badagliacca [41] reported that RV pressure and volume overload affect LV function, which may in turn affect RV function, with the clinical relevance of these observations being explored. Mauger et al. [42] found that RV dilation, LV reduction, and septal-lateral flattening were all associated with increased PR volume by analysing a biventricular atlas, suggesting that relationships between LV and RV morphometry and wall motion in PR patients have important clinical applications. However, the interaction between the LV and RV in PR conditions has not been thoroughly studied from a computational modelling perspective.

To address the aforementioned deficiencies, we propose the following FE human bi-ventricle model and simulate five cases with varying degrees of PR severity to analyse its effect on cardiac motion and functions. Building on our previous research on computational LV modelling [30], we incorporate a patient-specific bi-ventricle geometry and tune backflow from the main pulmonary artery to the RV to achieve realistic cardiac performance under different degrees of PR. We present comparisons of the simulated results with experimental studies and clinical observations, including ejection fractions of both the LV and RV, cardiac stress, and pressure ranges of the main pulmonary artery and aorta. RV dilation in PR cases is further compared with reported CMR data. Additionally, we compare long-axis and short-axis views of the bi-ventricle geometry as well as septal motion with the literature. In summary, this study introduces a 3D dynamic bi-ventricle model coupled with open-loop circulatory systems to investigate the effect of PR on the cardiac functions of the LV and RV as well as their interaction. Our model shows promise for predicting and assessing the impact of PR on cardiac functions.

2. Methods

The 3D human bi-ventricle model described herein is composed of the following components (see Fig. 1): a patient-specific bi-ventricle mesh, a commonly used myofibre structure, an up-to-date passive myocardium constitutive law, a modified active tension model for active contraction, an open-loop lumped parameter model for systemic circulation, and an open-loop lumped parameter model for the pulmonary circulation. The geometry of the patient-specific bi-ventricle is obtained through a process described in a previous study [43] that includes both the LV and RV. The study was approved by the National Research Ethics Services, and written consent was obtained before the CMR study. An in-house developed Matlab code is utilised to extract the endocardial and epicardial surfaces of the bi-ventricle based on CMR scans during early diastole when the cavity pressures are at their lowest. The geometry is meshed by ICEM (ANSYS, Inc. PA USA), as shown

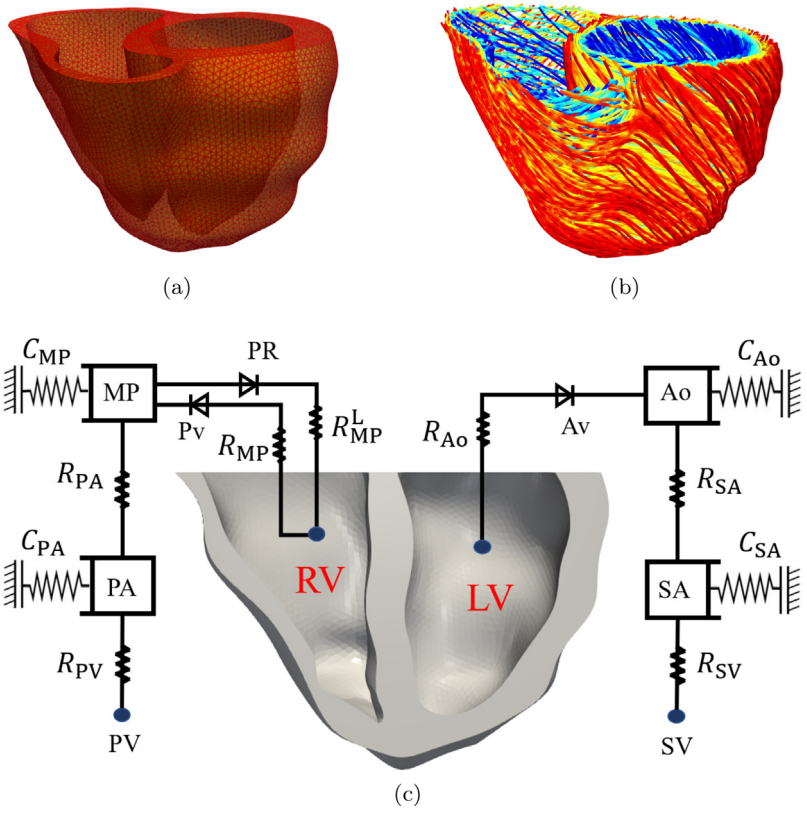

Fig. 1. A schematic illustration of the human bi-ventricle model. The bi-ventricle mesh (a) consists of 173,974 linear tetrahedral elements and 35,841 nodes, while the myofibre structure (b) is described by a rule-based method where the myofibre angle varies from -60° at the epicardium to 60° at the endocardium. In addition, the bi-ventricle cavities are coupled with systemic and pulmonary circulations that are represented by lumped parameter models (c). In this figure, LV refers to the left ventricle, Ao represents the aorta, SA stands for the systemic arteries, SV denotes the systemic veins, RV represents the right ventricle, MP is used for the main pulmonary artery, PA refers to the pulmonary arteries, and PV denotes the pulmonary veins. The unidirectional flow in the model is symbolized by the Diode symbols, whereas the pulmonary and aortic valves are denoted by the Diode symbols Pv and Av, respectively. The model also includes a PR valve, which regulates the absence of pulmonary regurgitation. In a non-pathological state, the PR valve remains closed, and the flow occurs only from the RV to the pulmonary arteries. R_{Ao} represents the resistance of the aortic valve, and R_{SA} denotes the resistance of the systemic arteries. R_{SV} represents a trivial resistance that allows the flow to drain in the systemic circulation. R_{MP} represents the resistance of the pulmonary valve in a healthy condition, while R_{PA} denotes the resistance of the pulmonary arteries. R_{PV} represents a trivial resistance that enables the flow to drain in the pulmonary circulation. C_{Ao} represents the compliance of the aorta, while C_{SA} represents the compliance of the systemic arteries. C_{MP} denotes the compliance of the main pulmonary artery, and C_{PA} represents the compliance of the pulmonary arteries. It is important to note that in this model, the severity of the pulmonary regurgitation is regulated by the resistance R^{L}_{MP}. When this resistance is reduced, there will be an increased retrograde flow of blood from the pulmonary arteries back to the RV, which corresponds to a greater degree of pulmonary regurgitation.

in Fig. 1 (a), which consists of 173,974 tetrahedral elements and 35,841 nodes. The corresponding myofibre architecture in Fig. 1 (b) is generated using a rule-based method [44]. In this model, the fibre rotation angles linearly vary from -60° at the epicardium to 60° at the endocardium, which is consistent with previous findings [20,45].

The LV and RV cavities are first enclosed using two-dimensional triangular surface elements as introduced in previous studies [21,22] so that they can be defined as fluid-filled cavities in ABAQUS. Next, the LV and RV cavities are connected to simplified open-loop lumped parameter systems representing the systemic circulation and the pulmonary circulation, respectively, as shown in Fig. 1 (c). The bi-ventricle model is coupled with the lumped parameter systems through the interaction of LV and RV cavity pressures, allowing the lumped parameter systems to provide accurate cavity pressures. Additional information regarding the relationship between pressure, volume, compliance, and resistance can be found in the supplementary materials. As shown in Fig. 1 (c), there is an additional PR valve controlling the one-way leakage from the main pulmonary artery to the RV. Under normal conditions, the flow occurs only from the RV to the main pulmonary artery when the RV cavity pressure exceeds the pressure in the main pulmonary artery. Conversely, when the RV cavity pressure is lower than the pressure in the main pulmonary artery, no flow can return to the RV cavity. However, in PR cases, the additional PR valve is included to allow unidirectional flow from the main pulmonary artery back to the RV cavity when the pressure in the main pulmonary artery exceeds that of the RV. In this study, the resistance R^{L}_{MP} is adjusted to achieve varying degrees of PR severity. Specifically, five cases are examined:

- $R^{L}_{MP} = 1000\,\text{MPa}\cdot\text{s/m}^3$ for the baseline case;
- $R^{L}_{MP} = 60\,\text{MPa}\cdot\text{s/m}^3$ for the mild case;
- $R^{L}_{MP} = 35\,\text{MPa}\cdot\text{s/m}^3$ for the moderate 1 case;
- $R^{L}_{MP} = 25\,\text{MPa}\cdot\text{s/m}^3$ for the moderate 2 case;
- $R^{L}_{MP} = 15\,\text{MPa}\cdot\text{s/m}^3$ for the severe case.

2.1. Passive constitutive law

The orthotropic hyperelastic model proposed by Holzapfel and Ogden [25], also known as the HO model, has been widely utilised in the computational cardiology community [22,32,46,47]. An important characteristic of this model is its incorporation of the microstructure of the myocardium. It introduces a local orthonormal coordinate system defined by the unit fibre direction $\mathbf{f}_0$, sheet direction $\mathbf{s}_0$, and sheet-normal direction $\mathbf{n}_0$. The strain energy function of the HO model is based on the invariants of the right

Cauchy-Green deformation tensor $\mathbf{C} = \mathbf{F}^{\mathrm{T}}\mathbf{F}$, where $\mathbf{F}$ is the deformation gradient tensor. The invariants $I_{(1,\,4\mathrm{f},\,4\mathrm{s},\,8\mathrm{fs})}$ are calculated by

$$I_1 = \mathrm{trace}(\mathbf{C}),\quad I_{4\mathrm{f}} = \mathbf{f}_0 \cdot (\mathbf{C}\mathbf{f}_0),\quad I_{4\mathrm{s}} = \mathbf{s}_0 \cdot (\mathbf{C}\,\mathbf{s}_0),\quad I_{8\mathrm{fs}} = \mathbf{f}_0 \cdot (\mathbf{C}\,\mathbf{s}_0). \tag{1}$$

The strain energy function can be expressed as:

$$\Psi = \Psi_{\mathrm{g}} + \Psi_{\mathrm{aniso}}, \tag{2}$$

where Ψ_{g} is the strain energy of the ground matrix, and Ψ_{aniso} accounts for the strain energy associated with the fibre direction and the sheet direction, as well as their interactions. Specifically,

$$\begin{aligned}
\Psi_{\mathrm{g}} &= \frac{a_{\mathrm{g}}}{2b_{\mathrm{g}}}\{\exp[b_{\mathrm{g}}(I_1 - 3)]\},\\
\Psi_{\mathrm{aniso}} &= \Psi_{\mathrm{aniso}}^{I_{4\mathrm{f}}} + \Psi_{\mathrm{aniso}}^{I_{4\mathrm{s}}} + \Psi_{\mathrm{aniso}}^{I_{8\mathrm{fs}}},
\end{aligned} \tag{3}$$

where

$$\begin{aligned}
\Psi_{\mathrm{aniso}}^{I_{4\mathrm{f}}} &= \frac{a_{\mathrm{f}}}{2b_{\mathrm{f}}}\{\exp[b_{\mathrm{f}}(I_{4\mathrm{f}} - 1)^2] - 1\}\,\mathcal{H}(I_{4\mathrm{f}} - 1),\\
\Psi_{\mathrm{aniso}}^{I_{4\mathrm{s}}} &= \frac{a_{\mathrm{s}}}{2b_{\mathrm{s}}}\{\exp[b_{\mathrm{s}}(I_{4\mathrm{s}} - 1)^2] - 1\}\,\mathcal{H}(I_{4\mathrm{s}} - 1),\\
\Psi_{\mathrm{aniso}}^{I_{8\mathrm{fs}}} &= \frac{a_{\mathrm{fs}}}{2b_{\mathrm{fs}}}[\exp(b_{\mathrm{fs}}I_{8\mathrm{fs}}^2) - 1],
\end{aligned} \tag{4}$$

in which $a_{(\mathrm{g,\,f,\,s,\,fs})}, b_{(\mathrm{g,\,f,\,s,\,fs})}$ are constant material parameters, $\mathcal{H}(\cdot)$ is the Heaviside step function to ensure that only stretched fibres can bear the load, e.g., $\mathcal{H}(I_{4\mathrm{f}} - 1) = 1$ when $I_{4\mathrm{f}} - 1 > 0$, otherwise $\mathcal{H}(I_{4\mathrm{f}} - 1) = 0$. The passive Cauchy stress tensor ($\boldsymbol{\sigma}^p$) derived from the strain energy function is

$$\begin{aligned}
\boldsymbol{\sigma}^p = \mathbf{F}\frac{\partial \Psi}{\partial \mathbf{F}} - p\mathbf{I} = 2J^{-1}[&\phi_1(\bar{\mathbf{B}} - \frac{1}{3}\bar{I}_1\mathbf{I}) + \phi_{4\mathrm{f}}(\hat{\mathbf{f}}_0 \otimes \hat{\mathbf{f}}_0 - \frac{1}{3}\bar{I}_{4\mathrm{f}}\mathbf{I})\\
&+ \phi_{4\mathrm{s}}(\hat{\mathbf{s}}_0 \otimes \hat{\mathbf{s}}_0 - \frac{1}{3}\bar{I}_{4\mathrm{s}}\mathbf{I})\\
&+ \frac{1}{2}\phi_{8\mathrm{fs}}(\hat{\mathbf{f}}_0 \otimes \hat{\mathbf{s}}_0 + \hat{\mathbf{s}}_0 \otimes \hat{\mathbf{f}}_0 - \frac{2}{3}\bar{I}_{8\mathrm{fs}}\mathbf{I})] - p\mathbf{I},
\end{aligned} \tag{5}$$

where $J = \det(\mathbf{F})$, $\phi_i = \partial\psi_{\mathrm{dev}}/\partial\bar{I}_i$, $i \in (1, 4\mathrm{f}, 4\mathrm{s}, 8\mathrm{fs})$, ψ_{dev} is the deviatoric part of the strain energy function, $\bar{I}_i$ are invariants calculated from the deviatoric part of the right Cauchy-Green tensor $\bar{\mathbf{C}} = J^{-2/3}\mathbf{C}$, $\bar{\mathbf{B}} = J^{-2/3}\mathbf{F}\mathbf{F}^{\mathrm{T}}$ is the deviatoric part of the left Cauchy-Green tensor, $\hat{\mathbf{f}}_0$ and $\hat{\mathbf{s}}_0$ are the unit vector in the current configuration of the fibre direction and the sheet direction, respectively, p is a Lagrange multiplier to ensure the incompressible constraint, and $\mathbf{I}$ is the second-order identity tensor.

2.2. Active tension model

The active tension (T_{a}) generated by myofibres during myocardial contraction is determined through a well-established time-varying elastance model [22,26,31], i.e.,

$$T_{\mathrm{a}}(t, l) = \frac{T_{\max}}{2}\,\frac{\mathrm{Ca}_0^2}{\mathrm{Ca}_0^2 + \mathrm{ECa}_{50}^2\,(l)}\,(1 - \cos\,(\omega(t, l))), \tag{6}$$

where $T_{\max}$ is the maximum isometric active tension, Ca_0 is the peak intra-cellular calcium, t is the time, and the length-dependent calcium sensitivity (ECa_{50}) is given by

$$\mathrm{ECa}_{50}(l) = \frac{\mathrm{Ca}_{0\max}}{\sqrt{e^{B(l - l_0)} - 1}}, \tag{7}$$

in which B and $\mathrm{Ca}_{0\max}$ are constants, l_0 is the minimum sarcomere length to produce active stress, and l is the deformed sarcomere length

$$l = l_r\sqrt{2E_{\mathrm{ff}} + 1}, \tag{8}$$

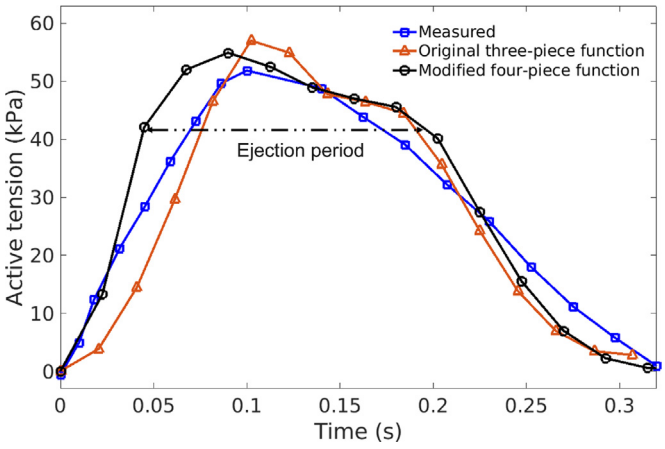

Fig. 2. Comparison of the active tension produced by the modified four-piece time function and the original three-piece time function [48], in relation to experimental data obtained from [49].

where l_r is the stress-free sarcomere length, and $E_{\mathrm{ff}} = \frac{1}{2}(\mathbf{f}_0 \cdot (\mathbf{C}\mathbf{f}_0) - 1)$ is the Lagrange strain in the myofibre direction. The time function after onset of contraction in Eq. (6) is

$$\omega(t, l) = \begin{cases} 2\pi\,\frac{t}{t_0} & \text{for} \quad 0 \leqslant t \leqslant t_{\mathrm{Iso}},\\ \pi + \frac{(t - t_0)(\pi - 2\pi\,t_{\mathrm{Iso}}/t_0)}{t_0 - t_{\mathrm{Iso}}} & \text{for} \quad t_{\mathrm{Iso}} < t \leqslant t_0,\\ \pi\,\frac{t - t_0 + t_r}{t_r} & \text{for} \quad t_0 < t \leqslant t_0 + t_r,\\ 0 & \text{for} \quad t > t_0 + t_r, \end{cases} \tag{9}$$

where $t_{\mathrm{Iso}} = 0.05$ s, t_0 is the time to peak tension, and t_r is the duration of relaxation, i.e.,

$$t_r(l) = ml + b, \tag{10}$$

where m and b are constants. It is worth noting that the piecewise time function, denoted as $\omega(t, l)$, in this study is composed of four pieces of linear functions, as opposed to the conventional three-piece time function [18,22,24]. The original three-piece time function was proposed by Tözeren [48] to account for the effect of activating calcium ions on fibre contraction. Fig. 2 displays a comparison of the active tension generated by the two different time functions as well as experimental data obtained from [49]. The current modification of $\omega(t, l)$ enhances the ascent rate of the active tension during the isovolumetric contraction phase, resulting in a reduced isovolumetric contraction time. Additionally, by utilising the original three-piece time function, the ejection time of the bi-ventricle model is found to be 0.12 s. However, the ejection time is extended to 0.16 s by incorporating the modified four-piece time function. The supplementary materials provide more information about the original time function.

Following the active stress approach [21,22], the total Cauchy stress can be expressed as follows

$$\boldsymbol{\sigma} = \boldsymbol{\sigma}^p + \boldsymbol{\sigma}^a, \tag{11}$$

where $\boldsymbol{\sigma}^p$ is the passive stress defined in Eq. (5) and $\boldsymbol{\sigma}^a$ is the active stress, i.e.,

$$\boldsymbol{\sigma}^a = T_{\mathrm{a}}\hat{\mathbf{f}} \otimes \hat{\mathbf{f}}. \tag{12}$$

Given this total Cauchy stress, the dynamics of the bi-ventricle are governed by

$$\begin{cases} \nabla \cdot \boldsymbol{\sigma} = 0, & \text{within the bi-ventricle wall domain,}\\ \boldsymbol{\sigma} \cdot \mathbf{n} = -P\mathbf{n}, & \text{on the endocardial surface,}\\ \boldsymbol{\sigma} \cdot \mathbf{n} = 0, & \text{on the epicardial surface,}\\ u_\theta = 0 \quad \text{and} \quad u_z = 0, & \text{on the LV basal plane,}\\ u_z = 0, & \text{on the RV basal plane,} \end{cases} \tag{13}$$

Table 1
Values of parameters utilised in the passive and active models.

	a_g (kPa)	b_g -	a_f (kPa)	b_f -	a_s (kPa)	b_s -	a_{fs} (kPa)	b_{fs} -
Passive constitutive law [30]								
LV	0.1731	5.1207	1.9344	0.2199	0.2143	0.0005	0.2665	2.5505
RV	0.3917	5.1207	4.400	0.2199	0.4850	0.0005	0.6031	2.5505

	m (s μm^{-1})	b (s)	l_0 (μ m)	B (μm^{-1})	Ca_0 (μM)	Ca_{0max} (μM)	T_{max} (kPa)	l_r (μm)
Active tension model [30]								
LV	1.0489	-1.429	1.58	4.750	4.35	4.35	130	1.85
RV	1.0489	-1.429	1.58	4.750	4.35	4.35	90	1.85

where **n** is the unit vector normal to the endocardial or epicardial surface, P is the pressure within the LV or RV cavity, u_θ and u_z are the displacement along the θ-axis and the z-axis (which correspond to the long axis direction of the heart) of the global cylinder coordinate system, respectively. In order to address the fact that the RV wall is thinner and more deformable than the LV wall, we have taken a cautious approach by limiting the long-axis displacement of the RV basal plane, which is consistent with the methodology used by Quarteroni et al. [33] and Guan et al. [24]. However, to ensure that the LV basal plane undergoes realistic expansion and contraction, we have further imposed a θ-axis constraint, which has been adopted by Thekkethil et al. [50]. It is important to note that in this study, the term "RV wall" refers to the RV-free wall, while the term "LV wall" encompasses both the septum wall and the LV-free wall. The utilisation of the global cylinder coordinate system facilitates us to characterize the even radial expansion and contraction of the basal plane of the LV. This enables the preservation of its circular shape and relatively uniform wall thickness, particularly in the septum region.

2.3. Implementation

The bi-ventricle model described above is solved using the FE method via ABAQUS 2018 (Dassault Systemes, Johnston RI, USA). The constitutive models are implemented through the ABAQUS VUMAT user subroutine. The fluid cavity and fluid exchange modulus provided by ABAQUS are further used to implement the lumped parameter circulatory systems.

The duration of a single cardiac cycle is taken to be 0.9 s, corresponding to a heart rate of 67 beats per minute. The simulation of 5 consecutive cardiac cycles requires approximately 80 hours to run on a Linux workstation equipped with 8 cores of 2.3 GHz CPU (Intel(R) Xeon(R) CPU E5-2699 v3) and 128 GB of memory. In the results section, we present the outcomes of the third cycle, which were found to be convergent. The values of the parameters used in the passive and active models are listed in Table 1, which have been adopted from a prior investigation [30].

The values of end-diastolic pressure (EDP), end-systolic pressure (ESP), end-diastolic volume (EDV), and end-systolic volume (ESV) are determined by the pressures and volumes of the LV and RV, respectively. Several cardiac function indicators are computed following studies in [17,51,52]. Specifically, the ejection fraction (EF) is calculated by

$$\text{EF} = (\text{EDV} - \text{ESV})/\text{EDV}. \tag{14}$$

The PR volume (PRV) is determined as the increment in the volume of the LV during diastole when the pressure of the RV drops [53]. The PR fraction (PRF) is calculated as the retrograde flow divided by the net antegrade flow [5,51], i.e.,

$$\text{PRF} = \text{PRV}/(\text{RVEDV} - \text{RVESV} - \text{PRV}). \tag{15}$$

The RV end-diastolic volume indexed by the body surface area (RVEDVi) is calculated as

$$\text{RVEDVi} = \text{RVEDV}/\text{BSA}, \tag{16}$$

where the body surface area (BSA) is 1.55 m^2 for the bi-ventricle geometry (obtained through email communication with the data holder).

3. Results

Simulated pressures for the aorta, the main pulmonary artery, the LV cavity, and the RV cavity in the baseline case are shown in Fig. 3. Specifically, as shown in Fig. 3 (a), the aortic pressure of the baseline case is from 69.2 mmHg to 109.6 mmHg, which agrees well with the normal range of the aortic pressure from 70.0 mmHg to 120.0 mmHg [54,55]. As shown in Fig. 3 (b), our simulated pulmonary pressure is from 6.1 mmHg to 27.8 mmHg, which is comparable with the normal range of the pulmonary pressure from 5 mmHg to 25 mmHg [56–58]. In Fig. 3 (c, d), the maximum pressures recorded in the LV and RV are 110.5 mmHg and 29.0 mmHg, respectively. The ejection phases of the LV and RV at baseline have been indicated by the vertical lines in Fig. 3. Specifically, the ejection phase of the LV at baseline spans from 0.43 s to 0.59 s, whereas the ejection phase of the RV takes place between 0.41 s and 0.60 s. It is noteworthy that the ejection time of the RV is longer compared to that of the LV, a finding that has been reported by Hirschfeld et al. [59].

In addition, Fig. 3 presents the pressure profiles of the four PR disease cases in the aorta, main pulmonary artery, LV cavity, and RV cavity. Overall, there is a substantial alteration in the pressure profiles from the baseline case to the disease cases. Specifically, the RV pressure and pulmonary pressure increase as a result of PR, while the LV pressure and aortic pressure decrease. In Fig. 3 (a), it can be observed that the aortic pressure continues to decrease from the baseline case to the severe case. The maximum aortic pressure of the severe case is 92.2 mmHg, which is 15.9% lower than the maximum aortic pressure of the baseline case (109.6 mmHg). Similarly, the minimum aortic pressure of the severe case is 61.5 mmHg, which is 11.1% lower than that of the baseline case (69.2 mmHg). This reduction in aortic pressure is primarily caused by the decrease in the peak pressure of the LV cavity, as illustrated in Fig. 3 (c). The maximum LV pressure of the severe case is 92.5 mmHg, which is 16.3% lower than the maximum LV pressure of the baseline case. Contrary to the changes observed in the LV pressure, as depicted in Fig. 3 (d), there is a significant increase in RV pressure from the baseline case to the severe case. The maximum RV pressure of the severe PR case is 42.5 mmHg, which is 46.6% higher than that of the baseline case (29.0 mmHg). This increase in the RV pressure leads to an increase in the peak pressure of the main pulmonary artery. As shown in Fig. 3 (b), the maximum pulmonary pressure of the severe case is 41.8 mmHg, which is 50.4% higher than that of the baseline case. The largest backflow in the severe case causes the pressure of the main pulmonary artery to drop quickly to its minimum at the time 0.24 s, even though its peak pressure is the highest. It is noteworthy that the pulmonary valve opens the earliest in the severe case because of its lowest pulmonary pressure and highest RV pressure. In addition, the earliest opening of the pulmonary valve in the severe case results in the longest ejection phase from the time 0.25 s to 0.60 s, which is 84.2% longer than that of the baseline case.

The PV loops of the LV and RV for the five cases are depicted in Fig. 4. In the baseline case, the simulated LV EDV is 115.6 mL, and the LV ESV is 45.6 mL, resulting in an EF of 60.5%. This EF value falls within the reported normal range of 50% to 65% for healthy individuals [60–62]. Additionally, the simulated EDV and ESV of the

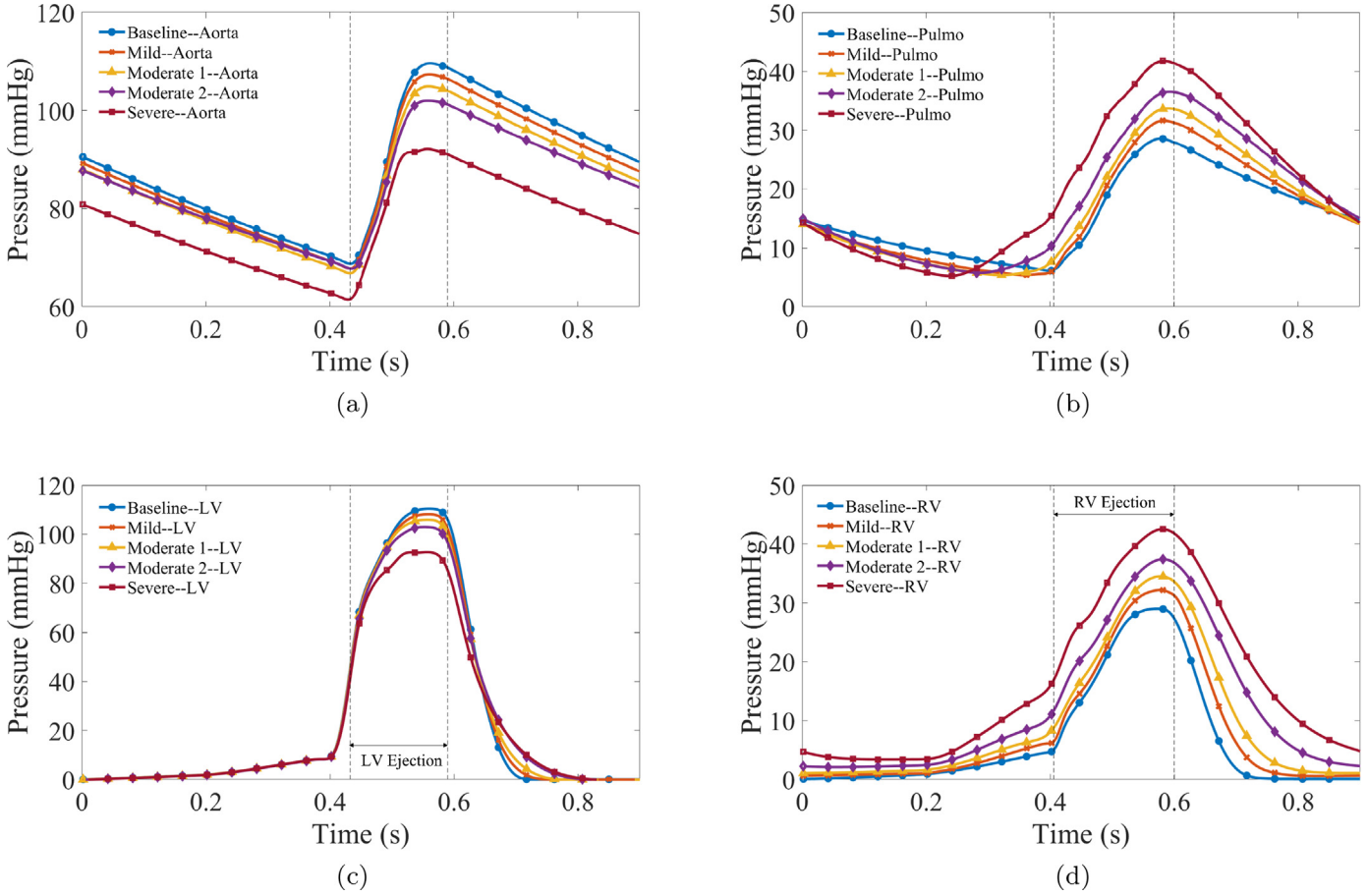

Fig. 3. Simulated pressure waveforms in a whole cardiac cycle of five cases with varying degrees of pulmonary regurgitation are shown in the aorta (a), the main pulmonary artery which is referred to as Pulmo (b), the left ventricle which is referred to as LV (c), and the right ventricle which is referred to as RV (d). It should be noted that the onset of systole occurs at 0.4 s. Additionally, the ejection phase of the LV of the baseline case is marked by the two vertical dashed lines in (a, c), while the ejection phase of the RV of the baseline case is marked by the two vertical lines in (b, d).

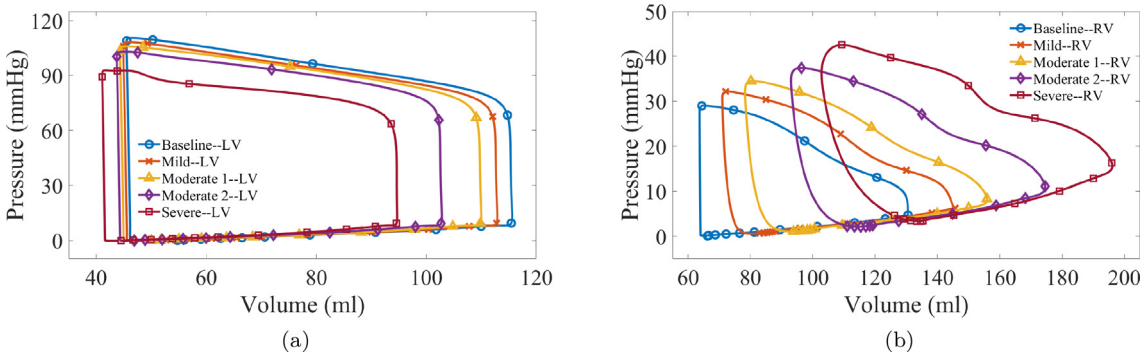

Fig. 4. Simulated pressure-volume loops for five cases with varying degrees of pulmonary regurgitation in the left ventricle (LV) (a) and the right ventricle (RV) (b).

RV for the baseline case are 132.5 mL and 63.8 mL, respectively, with an EF of 51.8%, which is consistent with the reported range of 52.3Ø6.2% (N=365) by Pfisterer et al. [63].

As illustrated in Fig. 4, varying degrees of PR severity greatly alter the PV loops of both the LV and RV. The PV loop of the LV shifts leftwards from the baseline case to the severe case, while the PV loop of the RV shifts rightwards. This phenomenon occurs due to the increasing dilation of the RV caused by PR. The RV dilation for patients with PR has been well-documented in numerous studies [9,16,17]. In our simulations, the RV EDV is the largest in the severe case, whereas the LV EDV is the smallest and experiences the most squeezing. Specifically, the RV EDV in the severe case increases by 50.3% compared to that of the baseline case, whereas the LV EDV in the severe case decreases by 18.1% compared with the baseline. Another observation is that all LV PV loops exhibit similar shapes, with the isovolumetric contraction and relaxation periods clearly marked by the vertical lines at ED and ES, respectively. However, the shapes of the RV PV loops in the disease cases differ from that of the baseline case as well as the LV PV loops. Specifically, the isovolumetric relaxation period disappears, and RV volume increases as pressure drops at the onset of diastole. Moreover, the isovolumetric contraction period shortens and eventually disappears. These characteristics of the RV PV loop have been observed in patients with PR in previous studies [64–66].

Table 2
Cardiac pump functions of the left ventricle (LV) and the right ventricle (RV) simulated for five cases of different degrees of pulmonary regurgitation.

Ventricles	Cases	EDP (mmHg)	ESP (mmHg)	EDV (mL)	ESV (mL)	EF	PRV (mL)	PRF
LV	Baseline	9.2	106.5	115.6	45.7	60.5%	-	-
	Mild	9.2	102.8	112.6	45.1	59.9%	-	-
	Moderate 1	9.1	104.3	110.0	44.6	59.5%	-	-
	Moderate 2	9.1	101.8	102.7	44.1	58.6%	-	-
	Severe	9.1	91.6	94.7	41.4	56.3%	-	-
RV	Baseline	4.6	27.7	132.5	63.8	51.8%	-	-
	Mild	6.2	31.4	145.5	71.1	51.1%	9.3	14.3%
	Moderate 1	7.5	33.8	156.4	78.5	49.8%	15.3	24.4%
	Moderate 2	10.0	37.0	175.0	93.1	46.8%	22.2	37.2%
	Severe	15.3	41.8	196.1	104.4	46.8%	30.8	50.6%

EDP = end-diastolic pressure; ESP = end-systolic pressure; EDV = end-diastolic volume; ESV = end-systolic volume; EF = ejection fraction; PRV = pulmonary regurgitation volume; PRF = pulmonary regurgitation fraction.

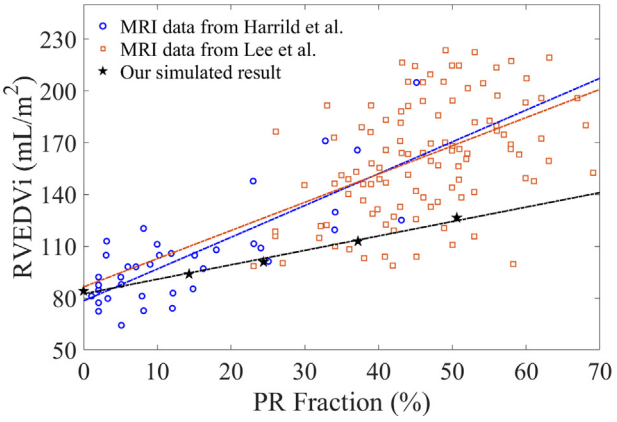

Fig. 5. Simulated end-diastolic volume of the right ventricle indexed by the body surface area (RVEDVi) versus pulmonary regurgitation (PR) fraction, compared with magnetic resonance imaging (MRI) data from [51,52]. The blue dashed line (RVEDVi = 1.77× PRF + 78.0, R = 0.79, p<0.001) is the linear regression of data from [51]. The orange dashed line (RVEDVi = 1.68× PRF + 84.2, R = 0.47, p<0.001) is the linear regression of data from [52]. Linear regression of our result is RVEDVi = 0.84× PRF + 82.5 with R = 0.99 and p<0.001. (For interpretation of the references to colour in this figure legend, the reader is referred to the web version of this article.)

The cardiac pump functions of the LV and RV for the five cases are summarized in Table 2, including EDP, ESP, EDV, ESV, EF, PRV, and PRF. The LV EDP remains relatively stable, but the RV EDP increases significantly. Specifically, the RV EDP of the severe case is 232.6% higher than that of the baseline case. On the other hand, the LV ESP of the severe case drops by 20.0% from the baseline case, while the RV ESP increases by 50.9%. Regarding the EF values, both the LV and RV EFs decline in disease cases, consistent with findings in previous studies [67,68]. The LV EF decreases by 6.9% from 60.5% in the baseline case to 56.3% in the severe case, and the RV EF decreases by 9.7% from 51.8% in the baseline case to 46.8% in the severe case. Notably, the RV EFs for the moderate PR-2 case and the severe case are the same, despite the severe case having a 12.1% larger RV EDV than the moderate PR-2 case. Furthermore, the four PR disease cases exhibit PRVs of 9.3 mL, 15.3 mL, 22.2 mL, and 30.8 mL, and PRFs of 14.3%, 24.4%, 37.2%, and 50.6%, respectively.

The simulated RVEDVi with respect to PRF is plotted in Fig. 5 with a comparison with CMR data reported by Harrild et al. [51] and Lee et al. [52]. The RVEDVi values for the five PR cases fall within the range of the reported CMR data. For instance, the RVEDVi for the severe case is 126.5 mL/m^2, which falls within the range of 110.0 mL/m^2 to 215.3 mL/m^2 reported by Lee et al. [52]. It should be noted that the CMR data are based on 41 and 66 patients, respectively, in the studies conducted by Harrild et al. [51] and Lee et al. [52].

The long-axis and short-axis views of the bi-ventricle geometry can be found in Fig. 6, showing LV and RV shapes and myofibre stress distributions in the five cases at ED and at ES, respectively. In the long-axis views at ED as shown in Fig. 6 (a), an evident increase in the RV cavity can be observed as PR becomes severe. This enlargement is attributed to the elevated backflow (PRV) and pressure within the RV cavity. Additionally, the motion of the interventricular septum can be observed, which has a right convexity in the baseline case [40]. With the increase of PRV, the septum bulges towards the LV, causing the squeeze of the LV. In Fig. 6 (b), the short-axis views at ED reveal that the shape of the LV cross-sectional cut plane is almost circular in the baseline case, but it transforms into a flattened D-shape in the severe PR case. Quantitatively, the distance between the septum and the LV free wall at ED reduces by 28.0% in the severe case, while the distance between the septum and the RV free wall increases by 29.4%, compared to the baseline case. While the shapes of the LV, septum, and RV undergo significant alterations at ED in the severe PR case, the changes in the shapes of the bi-ventricle are modest at ES. The septum is not clearly bulging toward the LV, from the long-axis views at ES as shown in Fig. 6 (c). However, from the short-axis views at ES as shown in Fig. 6 (d), RV dilation and the flattening of the LV cross-sectional cut plane can again be observed when PR becomes severe. At ES, the distance between the septum and the LV free wall is reduced by 5.7% in the severe case, while the distance between the septum and the RV free wall is increased by 49.6% compared to the baseline case. The motion of the septum and the flattening of the LV cross-sectional cut plane in the short-axis views have been reported in patients with PR or RV overload [40–42,69,70].

To further quantitatively measure the motion of the septum, we employ the Menger curvature [71]. Fig. 7 (a) shows the selection of three points (C_1, C_2, C_3) from the long-axis cut plane (in the middle of the bi-ventricle geometry) and two points (C_4, C_5) from the short-axis cut plane (at the equator plane of the bi-ventricle geometry). Specifically, C_1 is chosen at the midpoint of the septum at the base, C_2 at the intersection of the long-axis and short-axis cut planes, C_3 near the apex, and C_4 and C_5 near the junctions of the septum and the LV free wall. These points enabled us to measure the curvature of the septum from both the long-axis and short-axis views. The Menger curvature of the septum from the long-axis view is calculated by

$$\frac{4A}{|C_1 - C_2||C_2 - C_3||C_3 - C_1|}, \tag{17}$$

where A is the area of the triangle spanned by the three points and $|\cdot|$ is the Euclidean distance. The Menger curvature of the septum

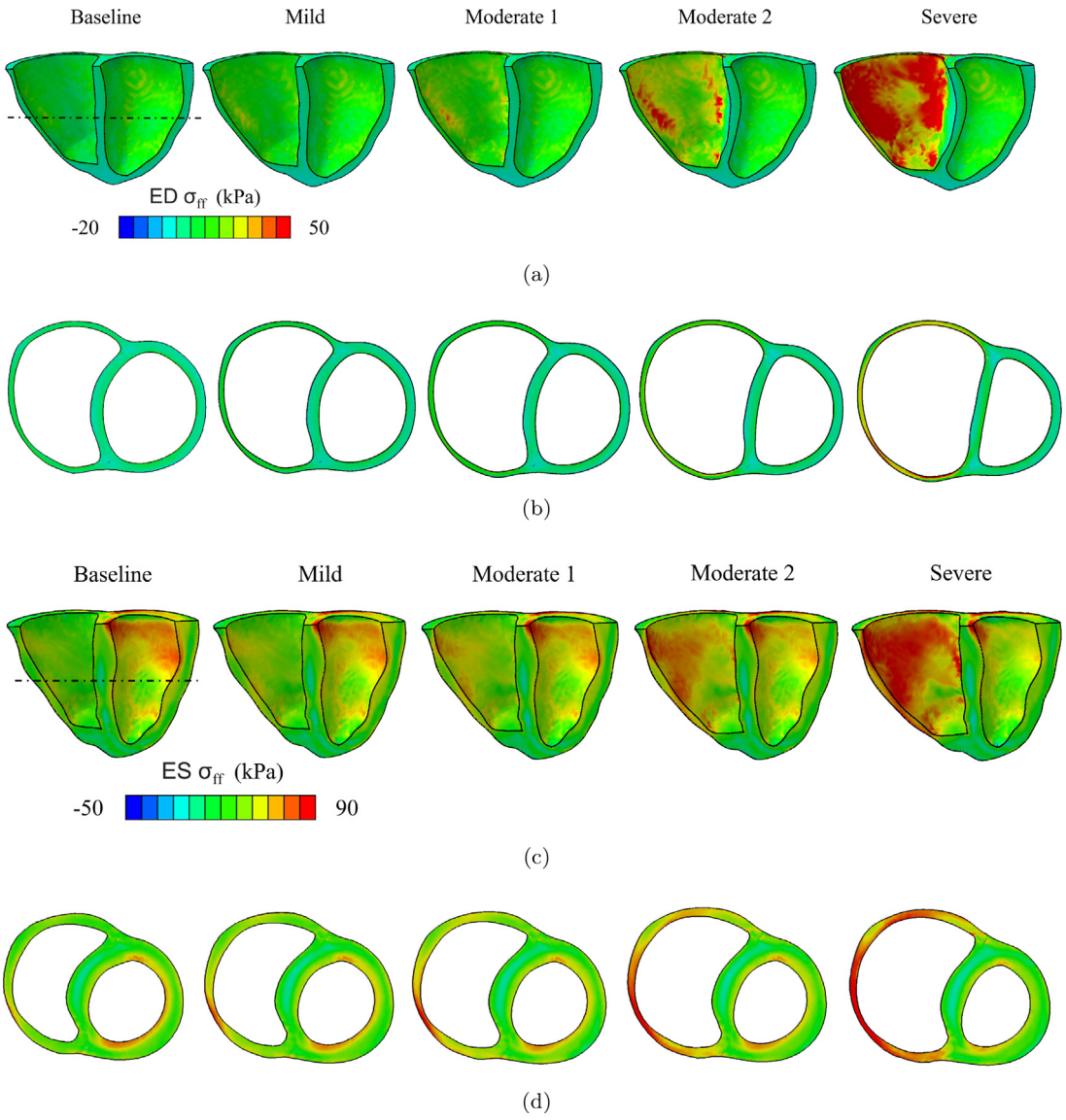

Fig. 6. Long-axis views, obtained through half cuts along the bi-ventricle geometry's long-axis, showing the left and right ventricular shapes and myofibre stress (σ_{ff}) distribution for five cases of different degrees of pulmonary regurgitation at end-diastole (ED) (a) and at end-systole (ES) (c). The dashed lines in (a, c) denote the position of the short-axis cut planes. Short-axis views, generated through cross-sectional cuts at the bi-ventricle geometry's equator plane, are shown at ED (b) and at ES (d).

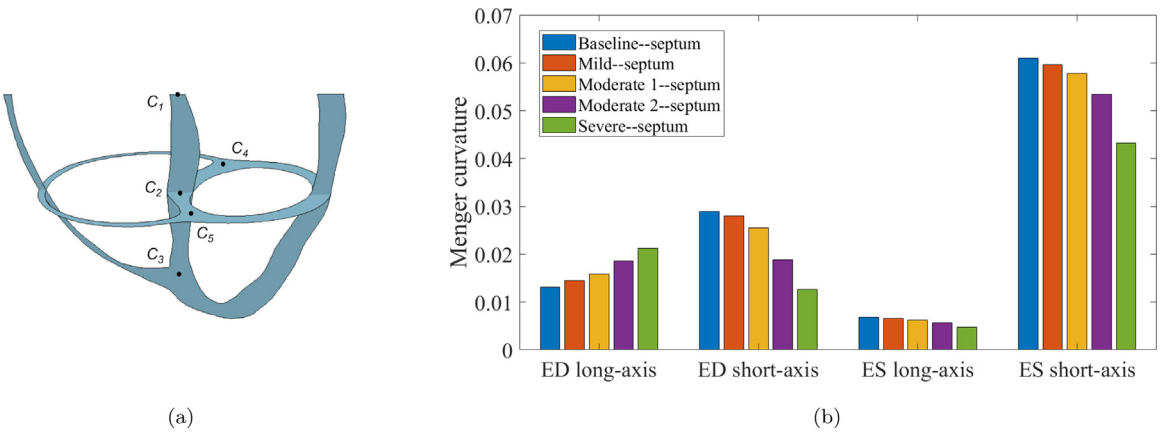

Fig. 7. Five points (a) selected from the septum's midline on both long-axis and short-axis cut planes for Menger curvature determination. The long-axis and short-axis Menger curvature of the septum at end-diastole (ED) and at end-systole (ES) for five cases with varying degrees of pulmonary regurgitation are shown in (b).

Table 3
Globally averaged myofibre stress ($\bar{\sigma}_{ff}$) and myofibre stretch ($\bar{\lambda}_f$) in the left ventricular wall (LV wall) and the right ventricular wall (RV wall) for five cases of different degrees of pulmonary regurgitation.

Positions	Cases	$\bar{\sigma}_{ff}$ (kPa)		$\bar{\lambda}_f$	
		ED	ES	ED	ES
LV wall	Baseline	3.7±18.1	37.7±31.4	1.18±0.07	0.92±0.03
	Mild	3.8±18.5	36.9±31.4	1.18±0.07	0.92±0.03
	Moderate 1	3.8±18.7	36.1±31.4	1.18±0.07	0.92±0.02
	Moderate 2	3.8±19.2	35.4±31.7	1.17±0.08	0.92±0.03
	Severe	4.3±20.3	31.6±32.0	1.17±0.09	0.92±0.03
RV wall	Baseline	2.7±12.1	24.6±28.4	1.12±0.07	0.94±0.06
	Mild	3.7±14.5	30.2±30.1	1.15±0.08	0.96±0.07
	Moderate 1	5.0±17.3	34.8±32.1	1.16±0.09	0.98±0.08
	Moderate 2	7.3±21.4	42.6±36.3	1.18±0.10	1.01±0.11
	Severe	10.9±26.5	50.5±41.7	1.21±0.11	1.03±0.12

Results are presented with standard deviations. ED = at the end of diastole; ES = at the end of systole. The RV wall is the RV-free wall, and the LV wall includes both the septum wall and the LV-free wall. The stress and stretch are volumetric-averaged over the LV wall or RV wall, respectively.

of the short-axis view is calculated as

$$\frac{4A}{|C_4 - C_2||C_2 - C_5||C_5 - C_4|}. \tag{18}$$

The computed long-axis and short-axis Menger curvature of the septum are shown in Fig. 7 (b). At ED, the long-axis Menger curvature increases by 61.5% from 0.013 at the baseline case to 0.021 at the severe case. The short-axis Menger curvature decreases by 55.2% from 0.029 at the baseline case to 0.013 at the severe case. At ES, the long-axis Menger curvature decreases by 28.6% from 0.007 at the baseline case to 0.005 at the severe case, and the short-axis Menger curvature decreases by 29.5% from 0.061 at the baseline case to 0.043 at the severe case.

The spatial distribution of myofibre stress in all five cases at ED and ES is presented in Fig. 6. In the baseline case at ED, as illustrated in Fig. 6 (a, b), the endocardial surface of the LV exhibits a green colour (corresponding to approximately 9 kPa) indicative of myofibre stress, while the epicardial surface shows a cyan-blue colour (approximately 3 kPa), consistent with the results reported in [72]. Notably, as PR becomes severe, there is a substantial increase in the myofibre stress on the endocardial surface of the RV at both ED and ES, as depicted in Fig. 6 (a, c). Additionally, Fig. 6 (d) demonstrates that the elevation in the myofibre stress of the RV wall is more pronounced in the thinner part of the RV wall.

The globally averaged myofibre stress ($\bar{\sigma}_{ff}$) and myofibre stretch ($\bar{\lambda}_f$) at ED and ES are obtained by computing the average over all elements of the LV or RV wall, weighted by the volume of the elements. For instance, the average myofibre stretch is calculated as

$$\bar{\lambda}_f = \frac{\sum_{i=1}^{n} (\lambda_f^i) V^i}{\sum_{i=1}^{n} V^i}, \tag{19}$$

where $\lambda_f^i = \sqrt{2E_{ff}^i + 1}$ is the myofibre stretch at the centroid of i^{th} element, E_{ff}^i is the Lagrange strain in the myofibre direction at the centroid of i^{th} element, V^i is the volume of i^{th} element, n is the total number of elements occupied by the LV wall or RV wall. Similarly, the averaged myofibre stress is computed using the Cauchy stress.

The values of the globally averaged myofibre stress ($\bar{\sigma}_{ff}$) and myofibre stretch ($\bar{\lambda}_f$) at ED and at ES are summarized in Table 3. The averaged LV myofibre stress increases by 16.2% from 3.7 kPa to 4.3 kPa at ED, while the averaged RV myofibre stress increases by 303.7% from 2.7 kPa to 10.9 kPa. A previous study by Tang et al. [38] showed comparable mean principal stress of the RV in a healthy group of 3.00 kPa and in a PR group of 7.31 kPa. Additionally, in Fig. 6 (a), the myofibre stress on the endocardial surface of the RV in the severe case is significantly higher than that of the LV. At ES, the averaged LV myofibre stress decreases by 16.2% from 37.7 kPa to 31.6 kPa, while the averaged RV myofibre stress increases by 105.3% from 24.6 kPa to 50.5 kPa. The decrease of the LV myofibre stress and the increase of the RV myofibre stress as PR becomes severe can be clearly observed in Fig. 6 (c). The averaged LV myofibre stretches change slightly at both ED and ES. In contrast, the averaged RV myofibre stretches increase by 8% at ED from 1.12 to 1.21 and by 10% at ES from 0.94 to 1.03.

4. Discussion

Our study demonstrated the benefits of employing a 3D computational bi-ventricle model to simulate PR, which enables the achievement of realistic bi-ventricle cardiac motion and functions by utilising updated myocardial constitutive laws, myofibre structure, and simplified open-loop lumped parameter models representing the systemic and pulmonary circulations. For the baseline case, the simulated pressures in the aorta and main pulmonary artery as well as the EF of both the LV and RV were all within the normal ranges reported for healthy individuals [54–57,60,63]. To simulate different degrees of PR severity, four disease cases were designed. Our simulated RVEDVi for these cases agreed well with CMR data published in the literature [51,52], as shown in Fig. 5. Furthermore, the motion of the septum and the shapes of the LV and RV cut planes were comparable with those reported in previous studies [40–42,70]. The comparison of the results obtained from this model with previously reported physiological ranges enabled us to examine the impact of PR on cardiac functions from a computational modelling perspective.

It is important to identify an optimal and easily obtained indicator for assessing the severity of PR and evaluating treatment for patients who have undergone RV outflow tract surgeries, particularly after TOF repair [13,17,73]. Previous studies have demonstrated the correlation between PR severity and RV dilation, especially the close relationship between PRF and RVEDVi [9,10,16,17,51,67]. This relationship has led to the use of RV volume obtained by CMR scans as a standard for determining the need for pulmonary valve replacement in patients with severe PR [17,74]. Our model obtained a nearly linear relationship between RVEDVi and PRF, which is consistent with these studies. However, it is noteworthy that the PRV for different degrees of PR in our simulations was not as large as reported by Wald et al. [17], who suggested that PRV provides a more accurate reflection of PR severity than PRF. They reported a median PRV of 19 mL/m^2 (range 0 - 63 mL/m^2) and a PRF of 29% (range 0–58%), considering a body surface area of 2.05 m^2. Nevertheless, due to the considerable variation in normal RV EDV across different individuals (ranging from 113 to 225 mL) [75,76], further research is needed to determine the reliability of PRV as an indicator of PR severity. Similarly, the ratio of PR duration to the diastolic duration and the ratio of diastolic and systolic time-velocity integrals may serve as useful measures. However, their correlation with PR severity is moderate and warrants further investigation as shown by Mercer-Rosa et al. [14].

The presence of PR can be easily identified by examining the PV loop of the RV. A normal PV loop for either the RV or the LV typically features two vertical lines representing the isovolumetric contraction and isovolumetric relaxation, indicating that the pulmonary valve and the aortic valve fully close without any leakage. In contrast, in cases of PR, the isovolumetric relaxation period disappears due to dysfunction of the pulmonary valve. Thus, as shown in Fig. 4 (b), the vertical line representing the isovolumetric relaxation was replaced by an oblique, slanting line, indicating backflow from the pulmonary arteries to the RV. The isovolumetric contraction period was also shortened and might dis-

appear altogether when PR becomes severe. These features of the PV loop of the RV have been observed in patients with PR [64–66], as well as in the PV loop of the LV in patients with aortic regurgitation [77–79]. Moreover, the LV PV loop shifted leftward from the baseline case to the severe case, while the RV PV loop shifted rightward. This was mostly because of the changes in the volume of the LV and RV resulting from RV dilation and LV compression. In addition, cardiac outputs (EF) of the LV and RV were both reduced in cases of PR, as previously reported in the literature [67,68,80]. Specifically, the LV EF decreased by 6.9% from the baseline case to the severe case, while the RV EF decreased by 9.7%.

The significant dilation of the RV due to severe PR led to a considerable deformation of the septum, resulting in a notable compression of the LV. This motion of the septum at ED was clearly visible in both the long-axis and short-axis views, as illustrated in Fig. 6 (a, b). Specifically, in the long-axis views, the septum was forced to bulge towards the LV in severe PR cases. Meanwhile, in the short-axis views, the LV cross-sectional cut plane that had a circular profile in the baseline case was flattened to a D-shaped profile in the presence of PR disease. These observations are consistent with previous studies [40–42,69,70]. As the short-axis scans can be easily accessed through CMR, the motion of the septum might serve as a readily-obtained indicator for assessing PR severity, which has been proposed in [40,81]. Furthermore, we calculated the Menger curvature of the septum, which can be easily obtained from three points and may have clinical utility. It is worth noting that the Menger curvature can measure two curvatures from the long-axis cut planes and short-axis cut planes, respectively, as the clinical implications of long-axis curvature and short-axis curvature may differ. Our computed Menger curvature revealed that a 50.6% PRF led to a 43.9% decrease in the short-axis curvature of the septum and a 61.5% increase in the long-axis curvature.

Previous research has suggested a significant increase in RV wall stress due to severe PR [10,74,82]. Our simulation results support this finding, as the severe case demonstrated average myofibre stress of the RV at ED which was 303.7% higher than that of the baseline case. Such a substantial increase in myofibre stress could result in higher intramyocardial pressure, which could impede coronary flow and reduce the perfusion of the RV wall. The impeding phenomenon of the intramyocardial pressure on coronary flow has been studied in the literature [83–87]. Additionally, the RV EDP of the severe PR case was 223.4% higher than that of the baseline case. This increase can be attributed to the backflow from the main pulmonary artery to the RV, which causes significant RV overload.

5. Model limitations and future perspectives

While our study demonstrated potential in simulating PR, several limitations must be addressed in future research. Firstly, it should be noted that although our model incorporates patient-specific geometry, it cannot be strictly classified as a patient-specific model. This is because the validation is based on physiological ranges in the literature rather than patient-specific experimental data. The lack of experimental data highlight a need for computational modelling studies to improve the translation of clinical imaging measurements into patient-specific computational models [23]. Additionally, our simulated results may be affected by variations in patient-specific geometry and a more realistic arrangement of myofibres. Future work could involve the reconstruction of additional patient-specific hearts to investigate the impact of different geometries on simulation results.

Secondly, our model can be further improved by replacing the current open-loop lumped parameter systems with more advanced models. Several sophisticated models have been developed, such as those discussed in [39,88,89], which offer refined techniques for synthesizing clinical inputs and representing circulatory systems. These advanced models can enhance the accuracy and reliability of PR simulations. Additionally, one-dimensional flow models can be integrated to incorporate the wave propagation phenomenon. Another important consideration is the inclusion of a realistic 3D pulmonary valve, composed of three equally sized semilunar cusps. The importance of computational heart valve models and their clinical impact can be found in a review [90], and various related computational models can be found in studies such as [91–94]. However, incorporating the pulmonary valve into simulations can be challenging, as it requires more detailed fluid-structure interaction analysis.

Lastly, we acknowledge the limitations of the boundary conditions employed in our model. The boundary conditions only restrict the long-axis displacement of the RV basal plane. Additionally, we have imposed a θ-axis constraint on the LV basal surface to prevent unrealistic deformation of the septum. However, these simplified boundary conditions do not fully represent the complex physiological conditions of the heart, particularly in light of the presence of the pericardium and upper chambers. Asner et al. [95] have discussed such simplified boundary conditions and proposed novel boundary conditions that introduce data-driven boundary energy terms. Moreover, Pfaller et al. [96] have demonstrated that using a parallel spring and dashpot acting in the normal direction to the epicardium as pericardium boundary conditions can result in more realistic cardiac mechanics simulations.

6. Conclusion

In this study, we developed a 3D computational human bi-ventricle model to investigate the effect of varying degrees of PR severity on cardiac functions, mechanical behaviour, and the interaction of the LV and RV. Our model incorporated a patient-specific bi-ventricle geometry, commonly used myofibre structure, and up-to-date passive and active models for myocardial mechanical properties. Additionally, we included open-loop systemic and pulmonary circulations in the bi-ventricular model and introduced flow leakage from the pulmonary arteries back to the RV to simulate PR disease cases. The baseline case was validated against normal physiological ranges for healthy subjects reported in the literature, including both the LV and RV ejection fractions and pressures of the main pulmonary artery and aorta. Furthermore, our simulated RV end-diastolic volumes in PR disease cases were comparable to reported CMR data. We also observed RV dilation secondary to PR at end-diastole in the long-axis and short-axis views of the bi-ventricle geometry, with RV end-diastolic volume increasing by 50.3% from the baseline to the severe PR case. Severe PR resulted in reduced ejection fractions for both the LV and RV and significantly elevated myofibre stress in the RV wall. Finally, the motion of the interventricular septum was consistent with the literature and quantitatively measured by the Menger curvature of the septum. The agreement of our simulated results with reported data demonstrates the success of our model development and its applicability to diseased hearts with PR and beyond. In conclusion, our model provides a computational means to investigate and better understand the impact of PR on cardiac motion and functions. Further simulations and adaptations of our model can be applied to the clinical assessment of PR and medical decision-making for the treatment of patients with severe PR.

Author Contributions

XY and YW were involved in the conception, design of the study, and interpretation of the results. YW ran simulations and provided data for analysis. XY drafted the manuscript and assisted

in conducting the data analysis. Both authors contributed to the article and approved the submitted version.

Funding

Y. Wang acknowledges funding from the Chinese Scholarship Council and the fee waiver from the University of Glasgow.

Declaration of Competing Interest

The authors declare that they have no conflict of interest.

Acknowledgments

The authors thank Dr. Debao Guan for the discussion and advice on developing the biomechanical ventricular model and Dr. Hao Gao for sharing the bi-ventricular mesh, patient information, the conceptualization of the leaking valve, and proofreading of the manuscript, and thank Prof. Xiaoyu Luo for the guidance and suggestions in cardiac modelling.

Supplementary material

Supplementary material associated with this article can be found, in the online version, at 10.1016/j.cmpb.2023.107600

References

[1] P. Lancellotti, C. Tribouilloy, A. Hagendorff, L. Moura, B.A. Popescu, E. Agricola, J.-L. Monin, L.A. Pierard, L. Badano, J.L. Zamorano, et al., European association of echocardiography recommendations for the assessment of valvular regurgitation. part 1: aortic and pulmonary regurgitation (native valve disease), Eur. J. Echocardiogr. 11 (3) (2010) 223–244.
[2] M. Berger, A. Haimowitz, A. Van Tosh, R.L. Berdoff, E. Goldberg, Quantitative assessment of pulmonary hypertension in patients with tricuspid regurgitation using continuous wave doppler ultrasound, J. Am. Coll. Cardiol. 6 (2) (1985) 359–365.
[3] D. Mutlak, D. Aronson, J. Lessick, S.A. Reisner, S. Dabbah, Y. Agmon, Functional tricuspid regurgitation in patients with pulmonary hypertension: is pulmonary artery pressure the only determinant of regurgitation severity? Chest 135 (1) (2009) 115–121.
[4] Y. Topilsky, A. Khanna, T. Le Tourneau, S. Park, H. Michelena, R. Suri, D.W. Mahoney, M. Enriquez-Sarano, Clinical context and mechanism of functional tricuspid regurgitation in patients with and without pulmonary hypertension, Circulation: Cardiovasc. Imag. 5 (3) (2012) 314–323.
[5] S.A. Rebergen, J. Chin, J. Ottenkamp, E. Van der Wall, A. De Roos, Pulmonary regurgitation in the late postoperative follow-up of tetralogy of Fallot. volumetric quantitation by nuclear magnetic resonance velocity mapping, Circulation 88 (5) (1993) 2257–2266.
[6] B. Bouzas, P.J. Kilner, M.A. Gatzoulis, Pulmonary regurgitation: not a benign lesion, Eur. Heart J. 26 (5) (2005) 433–439.
[7] E.A. Shinebourne, S.V. Babu-Narayan, J.S. Carvalho, Tetralogy of Fallot: from fetus to adult, Heart 92 (9) (2006) 1353–1359.
[8] R.R. Chaturvedi, A.N. Redington, Pulmonary regurgitation in congenital heart disease, Heart 93 (7) (2007) 880–889.
[9] A. Frigiola, V. Tsang, J. Nordmeyer, P. Lurz, C. van Doorn, A.M. Taylor, P. Bonhoeffer, M. de Leval, Current approaches to pulmonary regurgitation, Eur. J. Cardio-Thoracic Surg. 34 (3) (2008) 576–581.
[10] T. Geva, B.M. Sandweiss, K. Gauvreau, J.E. Lock, A.J. Powell, Factors associated with impaired clinical status in long-term survivors of tetralogy of Fallot repair evaluated by magnetic resonance imaging, J. Am. Coll. Cardiol. 43 (6) (2004) 1068–1074.
[11] M.D. Puchalski, B. Askovich, C.T. Sower, R.V. Williams, L.L. Minich, L.Y. Tani, Pulmonary regurgitation: determining severity by echocardiography and magnetic resonance imaging, Congenit. Heart. Dis. 3 (3) (2008) 168–175.
[12] F.-P. Mongeon, W.B. Ali, P. Khairy, I. Bouhout, J. Therrien, R.M. Wald, F. Dallaire, P.-L. Bernier, N. Poirier, A. Dore, et al., Pulmonary valve replacement for pulmonary regurgitation in adults with tetralogy of Fallot: a meta-analysisa report for the writing committee of the 2019 update of the canadian cardiovascular society guidelines for the management of adults with congenital heart disease, Canad. J. Cardiol. 35 (12) (2019) 1772–1783.
[13] W. Li, P.A. Davlouros, P.J. Kilner, D.J. Pennell, D. Gibson, M.Y. Henein, M.A. Gatzoulis, Doppler-echocardiographic assessment of pulmonary regurgitation in adults with repaired tetralogy of Fallot: comparison with cardiovascular magnetic resonance imaging, Am. Heart J. 147 (1) (2004) 165–172.
[14] L. Mercer-Rosa, W. Yang, S. Kutty, J. Rychik, M. Fogel, E. Goldmuntz, Quantifying pulmonary regurgitation and right ventricular function in surgically repaired tetralogy of Fallot: a comparative analysis of echocardiography and magnetic resonance imaging, Circulation: Cardiovasc. Imag. 5 (5) (2012) 637–643.
[15] C.K. Silversides, G.R. Veldtman, J. Crossin, N. Merchant, G.D. Webb, B.W. McCrindle, S.C. Siu, J. Therrien, Pressure half-time predicts hemodynamically significant pulmonary regurgitation in adult patients with repaired tetralogy of Fallot, J. Am. Soc. Echocardiogr. 16 (10) (2003) 1057–1062.
[16] P.A. Davlouros, A.A. Karatza, M.A. Gatzoulis, D.F. Shore, Timing and type of surgery for severe pulmonary regurgitation after repair of tetralogy of Fallot, Int. J. Cardiol. 97 (2004) 91–101.
[17] R.M. Wald, A.N. Redington, A. Pereira, Y.L. Provost, N.S. Paul, E.N. Oechslin, C.K. Silversides, Refining the assessment of pulmonary regurgitation in adults after tetralogy of Fallot repair: should we be measuring regurgitant fraction or regurgitant volume? Eur. Heart J. 30 (3) (2009) 356–361.
[18] J.C. Walker, M.B. Ratcliffe, P. Zhang, A.W. Wallace, B. Fata, E.W. Hsu, D. Saloner, J.M. Guccione, MRI-Based finite-element analysis of left ventricular aneurysm, Am. J. Physiol.-Heart Circulatory Physiol. 289 (2) (2005) H692–H700.
[19] S.M. Szilágyi, L. Szilágyi, Z. Benyó, A patient specific electro-mechanical model of the heart, Comput. Methods Programs Biomed. 101 (2) (2011) 183–200.
[20] H. Wang, H. Gao, X. Luo, C. Berry, B. Griffith, R. Ogden, T. Wang, Structure-based finite strain modelling of the human left ventricle in diastole, Int. J. Numer. Method Biomed. Eng. 29 (1) (2013) 83–103.
[21] B. Baillargeon, N. Rebelo, D.D. Fox, R.L. Taylor, E. Kuhl, The living heart project: a robust and integrative simulator for human heart function, Eur. J. Mech.-A/Solids 48 (2014) 38–47.
[22] K.L. Sack, E. Aliotta, D.B. Ennis, J.S. Choy, G.S. Kassab, J.M. Guccione, T. Franz, Construction and validation of subject-specific biventricular finite-element models of healthy and failing swine hearts from high-resolution DT-MRI, Front. Physiol. 9 (2018) 539.
[23] S.A. Niederer, J. Lumens, N.A. Trayanova, Computational models in cardiology, Nat. Rev. Cardiol. 16 (2) (2019) 100–111.
[24] D. Guan, J. Yao, X. Luo, H. Gao, Effect of myofibre architecture on ventricular pump function by using a neonatal porcine heart model: from DT-MRI to rule-based methods, R. Soc. Open Sci. 7 (4) (2020) 191655.
[25] G.A. Holzapfel, R.W. Ogden, Constitutive modelling of passive myocardium: a structurally based framework for material characterization, Philos. Trans. R. Soc. A: 367 (1902) (2009) 3445–3475.
[26] J. Guccione, A. McCulloch, Mechanics of active contraction in cardiac muscle: part iconstitutive relations for fiber stress that describe deactivation, J. Biomech. Eng. 115 (1) (1993) 72–81.
[27] J.M. Guccione, L. Waldman, A.D. McCulloch, Mechanics of active contraction in cardiac muscle: part II cylindrical models of the systolic left ventricle, J. Biomech. Eng. 115 (1) (1993) 82–90.
[28] S. Göktepe, E. Kuhl, Electromechanics of the heart: a unified approach to the strongly coupled excitation–contraction problem, Comput. Mech. 45 (2) (2010) 227–243.
[29] D. Guan, Y. Mei, L. Xu, L. Cai, X. Luo, H. Gao, Effects of dispersed fibres in myocardial mechanics, part i: passive response, Math. Biosci. Eng. (2022).
[30] D. Guan, Y. Wang, L. Xu, L. Cai, X. Luo, H. Gao, Effects of dispersed fibres in myocardial mechanics, part ii: active response, Math. Biosci. Eng. 19 (4) (2022) 4101–4119.
[31] A.D. Wisneski, Y. Wang, T. Deuse, A.C. Hill, S. Pasta, K.L. Sack, J. Yao, J.M. Guccione, Impact of aortic stenosis on myofiber stress: translational application of left ventricle-aortic coupling simulation, Front. Physiol. (2020) 1157.
[32] A.D. Wisneski, Y. Wang, S. Cutugno, S. Pasta, A. Stroh, J. Yao, T.C. Nguyen, V.S. Mahadevan, J.M. Guccione, Left ventricle biomechanics of low-flow, low–gradient aortic stenosis: a patient-specific computational model, Front. Physiol. (2022) 587.
[33] A. Quarteroni, T. Lassila, S. Rossi, R. Ruiz-Baier, Integrated heartcoupling multiscale and multiphysics models for the simulation of the cardiac function, Comput. Methods Appl. Mech. Eng. 314 (2017) 345–407.
[34] K. Mangion, H. Gao, D. Husmeier, X. Luo, C. Berry, Advances in computational modelling for personalised medicine after myocardial infarction, Heart 104 (7) (2018) 550–557.
[35] M. Peirlinck, F.S. Costabal, J. Yao, J. Guccione, S. Tripathy, Y. Wang, D. Ozturk, P. Segars, T. Morrison, S. Levine, et al., Precision medicine in human heart modeling, Biomech. Model. Mechanobiol. (2021) 1–29.
[36] D. Tang, C. Yang, T. Geva, G. Gaudette, P.J. Del Nido, Multi-physics MRI-based two-layer fluid–structure interaction anisotropic models of human right and left ventricles with different patch materials: cardiac function assessment and mechanical stress analysis, Comput. Struct. 89 (11–12) (2011) 1059–1068.
[37] D. Tang, P.J. Del Nido, C. Yang, H. Zuo, X. Huang, R.H. Rathod, V. Gooty, A. Tang, Z. Wu, K.L. Billiar, et al., Patient-specific MRI-based right ventricle models using different zero-load diastole and systole geometries for better cardiac stress and strain calculations and pulmonary valve replacement surgical outcome predictions, PLoS ONE 11 (9) (2016) e0162986.
[38] D. Tang, H. Zuo, C. Yang, Z. Wu, X. Huang, R.H. Rathod, A. Tang, K.L. Billiar, T. Geva, Comparison of right ventricle morphological and mechanical characteristics for healthy and patients with tetralogy of Fallot: an in vivo MRI-based modeling study, Mol. Cell. Biomech.: MCB 14 (3) (2017) 137.
[39] M. Gusseva, T. Hussain, C.H. Friesen, P. Moireau, A. Tandon, C. Patte, M. Genet, K. Hasbani, G. Greil, D. Chapelle, et al., Biomechanical modeling to inform pulmonary valve replacement in tetralogy of Fallot patients after complete repair, Canad. J. Cardiol. 37 (11) (2021) 1798–1807.
[40] C. Méndez, R. Soler, E. Rodriguez, M. López, L. Álvarez, N. Fernández, L. Montserrat, Magnetic resonance imaging of abnormal ventricular septal motion in heart diseases: a pictorial review, Insights Imag. 2 (4) (2011) 483–492.

[41] R. Naeije, R. Badagliacca, The overloaded right heart and ventricular interdependence, Cardiovasc. Res. 113 (12) (2017) 1474–1485.
[42] C.A. Mauger, S. Govil, R. Chabiniok, K. Gilbert, S. Hegde, T. Hussain, A.D. McCulloch, C.J. Occleshaw, J. Omens, J.C. Perry, et al., Right-left ventricular shape variations in tetralogy of Fallot: associations with pulmonary regurgitation, J. Cardiovasc. Magn. Reson. 23 (1) (2021) 1–14.
[43] H. Gao, A. Aderhold, K. Mangion, X. Luo, D. Husmeier, C. Berry, Changes and classification in myocardial contractile function in the left ventricle following acute myocardial infarction, J. R. Soc. Interface 14 (132) (2017) 20170203.
[44] J.D. Bayer, R.C. Blake, G. Plank, N.A. Trayanova, A novel rule-based algorithm for assigning myocardial fiber orientation to computational heart models, Ann. Biomed. Eng. 40 (10) (2012) 2243–2254.
[45] S. Nielles-Vallespin, C. Mekkaoui, P. Gatehouse, T.G. Reese, J. Keegan, P.F. Ferreira, S. Collins, P. Speier, T. Feiweier, R. De Silva, et al., In vivo diffusion tensor MRI of the human heart: reproducibility of breath-hold and navigator-based approaches, Magn. Reson. Med. 70 (2) (2013) 454–465.
[46] H. Gao, H. Wang, C. Berry, X. Luo, B.E. Griffith, Quasi-static image-based immersed boundary-finite element model of left ventricle under diastolic loading, Int. J. Numer. Method Biomed. Eng. 30 (11) (2014) 1199–1222.
[47] D. Guan, X. Luo, H. Gao, Constitutive modelling of soft biological tissue from ex vivo to in vivo: myocardium as an example, in: International Conference by Center for Mathematical Modeling and Data Science, Osaka University, Springer, 2020, pp. 3–14.
[48] A. Tözeren, Continuum rheology of muscle contraction and its application to cardiac contractility, Biophys. J. 47 (3) (1985) 303–309.
[49] P. Janssen, P.P. de Tombe, Uncontrolled sarcomere shortening increases intracellular ca2+ transient in rat cardiac trabeculae, Am. J. Physiol.-Heart Circul. Physiol. 272 (4) (1997) H1892–H1897.
[50] N. Thekkethil, S. Rossi, H. Gao, S.I.H. Richardson, B.E. Griffith, X. Luo, A stabilized linear finite element method for anisotropic poroelastodynamics with application to cardiac perfusion, Comput. Methods Appl. Mech. Eng. 405 (2023) 115877.
[51] D.M. Harrild, A.J. Powell, T.X. Trang, T. Geva, J.E. Lock, J. Rhodes, D.B. McElhinney, Long-term pulmonary regurgitation following balloon valvuloplasty for pulmonary stenosis: risk factors and relationship to exercise capacity and ventricular volume and function, J. Am. Coll. Cardiol. 55 (10) (2010) 1041–1047.
[52] C. Lee, Y.M. Kim, C.-H. Lee, J.G. Kwak, C.S. Park, J.Y. Song, W.-S. Shim, E.Y. Choi, S.Y. Lee, J.S. Baek, Outcomes of pulmonary valve replacement in 170 patients with chronic pulmonary regurgitation after relief of right ventricular outflow tract obstruction: implications for optimal timing of pulmonary valve replacement, J. Am. Coll. Cardiol. 60 (11) (2012) 1005–1014.
[53] T. Bove, K. Vandekerckhove, S. Bouchez, P. Wouters, P. Somers, G. Van Nooten, Role of myocardial hypertrophy on acute and chronic right ventricular performance in relation to chronic volume overload in a porcine model: relevance for the surgical management of tetralogy of Fallot, J. Thorac. Cardiovasc. Surg. 147 (6) (2014) 1956–1965.
[54] R. Erbel, F. Alfonso, C. Boileau, O. Dirsch, B. Eber, A. Haverich, H. Rakowski, J. Struyven, K. Radegran, U. Sechtem, et al., Diagnosis and management of aortic dissection: task force on aortic dissection, european society of cardiology, Eur. Heart J. 22 (18) (2001) 1642–1681.
[55] P. Reymond, N. Westerhof, N. Stergiopulos, Systolic hypertension mechanisms: effect of global and local proximal aorta stiffening on pulse pressure, Ann. Biomed. Eng. 40 (3) (2012) 742–749.
[56] B.M. McQuillan, M.H. Picard, M. Leavitt, A.E. Weyman, Clinical correlates and reference intervals for pulmonary artery systolic pressure among echocardiographically normal subjects, Circulation 104 (23) (2001) 2797–2802.
[57] V.V. McLaughlin, S.L. Archer, D.B. Badesch, R.J. Barst, H.W. Farber, J.R. Lindner, M.A. Mathier, M.D. McGoon, M.H. Park, R.S. Rosenson, et al., A report of the american college of cardiology foundation task force on expert consensus documents and the american heart association, Circulation 119 (16) (2009) 2250–2294.
[58] A.V. Noordegraaf, K.M. Chin, F. Haddad, P.M. Hassoun, A.R. Hemnes, S.R. Hopkins, S.M. Kawut, D. Langleben, J. Lumens, R. Naeije, Pathophysiology of the right ventricle and of the pulmonary circulation in pulmonary hypertension: an update, Eur. Respirat. J. 53 (1) (2019).
[59] S. Hirschfeld, R. Meyer, D.C. Schwartz, J. Korfhagen, S. Kaplan, Measurement of right and left ventricular systolic time intervals by echocardiography, Circulation 51 (2) (1975) 304–309.
[60] G. Mahadevan, R. Davis, M. Frenneaux, F. Hobbs, G. Lip, J. Sanderson, M. Davies, Left ventricular ejection fraction: are the revised cut-off points for defining systolic dysfunction sufficiently evidence based? Heart 94 (4) (2008) 426–428.
[61] J.J. Feher, Quantitative Human Physiology: An Introduction, Academic press, 2017.
[62] R.M. Lang, L.P. Badano, V. Mor-Avi, J. Afilalo, A. Armstrong, L. Ernande, F.A. Flachskampf, E. Foster, S.A. Goldstein, T. Kuznetsova, et al., Recommendations for cardiac chamber quantification by echocardiography in adults: an update from the american society of echocardiography and the european association of cardiovascular imaging, Eur. Heart J.-Cardiovasc. Imag. 16 (3) (2015) 233–271.
[63] M. Pfisterer, A. Battler, B. Zaret, Range of normal values for left and right ventricular ejection fraction at rest and during exercise assessed by radionuclide angiocardiography, Eur. Heart J. 6 (8) (1985) 647–655.
[64] A.N. Redington, P.J. Oldershaw, E.A. Shinebourne, M.L. Rigby, A new technique for the assessment of pulmonary regurgitation and its application to the assessment of right ventricular function before and after repair of tetralogy of Fallot, Heart 60 (1) (1988) 57–65.
[65] R.R. Chaturvedi, P.J. Kilner, P.A. White, A. Bishop, R. Szwarc, A.N. Redington, Increased airway pressure and simulated branch pulmonary artery stenosis increase pulmonary regurgitation after repair of tetralogy of Fallot: real–time analysis with a conductance catheter technique, Circulation 95 (3) (1997) 643–649.
[66] C. Yerebakan, C. Klopsch, S. Prietz, J. Boltze, B. Vollmar, A. Liebold, G. Steinhoff, E. Sandica, Pressure-volume loops: feasible for the evaluation of right ventricular function in an experimental model of acute pulmonary regurgitation? Interact. Cardiovasc. Thorac. Surg. 9 (2) (2009) 163–168.
[67] M. Abd El Rahman, H. Abdul-Khaliq, M. Vogel, V. Alexi-Meskishvili, M. Gutberlet, P. Lange, Relation between right ventricular enlargement, qrs duration, and right ventricular function in patients with tetralogy of Fallot and pulmonary regurgitation after surgical repair, Heart 84 (4) (2000) 416–420.
[68] P.A. Davlouros, P.J. Kilner, T.S. Hornung, W. Li, J.M. Francis, J.C. Moon, G.C. Smith, T. Tat, D.J. Pennell, M.A. Gatzoulis, Right ventricular function in adults with repaired tetralogy of Fallot assessed with cardiovascular magnetic resonance imaging: detrimental role of right ventricular outflow aneurysms or akinesia and adverse right-to-left ventricular interaction, J. Am. Coll. Cardiol. 40 (11) (2002) 2044–2052.
[69] E.K. Louie, S. Rich, S. Levitsky, B.H. Brundage, Doppler echocardiographic demonstration of the differential effects of right ventricular pressure and volume overload on left ventricular geometry and filling, J. Am. Coll. Cardiol. 19 (1) (1992) 84–90.
[70] F.H. Sheehan, S. Ge, G.W. Vick III, K. Urnes, W.S. Kerwin, E.L. Bolson, T. Chung, J.P. Kovalchin, D.J. Sahn, M. Jerosch-Herold, et al., Three-dimensional shape analysis of right ventricular remodeling in repaired tetralogy of Fallot, Am. J. Cardiol. 101 (1) (2008) 107–113.
[71] J.C. Léger, Menger curvature and rectifiability, Ann. Math. 149 (3) (1999) 831–869.
[72] M. Genet, L.C. Lee, R. Nguyen, H. Haraldsson, G. Acevedo-Bolton, Z. Zhang, L. Ge, K. Ordovas, S. Kozerke, J.M. Guccione, Distribution of normal human left ventricular myofiber stress at end diastole and end systole: a target for in silico design of heart failure treatments, J. Appl. Physiol. 117 (2) (2014) 142–152.
[73] A.N. Redington, Determinants and assessment of pulmonary regurgitation in tetralogy of Fallot: practice and pitfalls, Cardiol. Clin. 24 (4) (2006) 631–639.
[74] M.A. El-Harasis, H.M. Connolly, W.R. Miranda, M.Y. Qureshi, N. Sharma, M. Al-Otaibi, C.V. DeSimone, A. Egbe, Progressive right ventricular enlargement due to pulmonary regurgitation: clinical characteristics of a æ low-risk g group, Am. Heart J. 201 (2018) 136–140.
[75] S. Kovalova, J. Necas, J. Vespalec, What is a æ normal g right ventricle? European Journal of Echocardiography 7 (4) (2006) 293–297.
[76] A.L. Eastman, D.A. Rosenbaum, E. Thal, The Parkland Trauma Handbook E–Book: Mobile Medicine Series, Elsevier Health Sciences, 2008.
[77] O. Gaemperli, P. Biaggi, R. Gugelmann, M. Osranek, J.J. Schreuder, I. Bühler, D. Sürder, T.F. Lüscher, C. Felix, D. Bettex, et al., Real-time left ventricular pressure-volume loops during percutaneous mitral valve repair with the mitraclip system, Circulation 127 (9) (2013) 1018–1027.
[78] A. Paul, S. Das, Valvular heart disease and anaesthesia, Indian J. Anaesth. 61 (9) (2017) 721.
[79] M.B. Bastos, D. Burkhoff, J. Maly, J. Daemen, C.A. den Uil, K. Ameloot, M. Lenzen, F. Mahfoud, F. Zijlstra, J.J. Schreuder, et al., Invasive left ventricle pressure–volume analysis: overview and practical clinical implications, Eur. Heart J. 41 (12) (2020) 1286–1297.
[80] R.A. Niezen, W.A. Helbing, E. Van der Wall, R. Van der Geest, S.A. Rebergen, A. De Roos, Biventricular systolic function and mass studied with mr imaging in children with pulmonary regurgitation after repair for tetralogy of Fallot, Radiology 201 (1) (1996) 135–140.
[81] W.A. Zoghbi, M. Enriquez-Sarano, E. Foster, P.A. Grayburn, C.D. Kraft, R.A. Levine, P. Nihoyannopoulos, C.M. Otto, M.A. Quinones, H. Rakowski, et al., Recommendations for evaluation of the severity of native valvular regurgitation with two-dimensional and doppler echocardiography, J. Am. Soc. Echocardiogr. 16 (7) (2003) 777–802.
[82] A. Frigiola, A. Redington, S. Cullen, M. Vogel, Pulmonary regurgitation is an important determinant of right ventricular contractile dysfunction in patients with surgically repaired tetralogy of Fallot, Circulation 110 (11_suppl_1) (2004) II–153.
[83] J. Hoffman, Determinants and prediction of transmural myocardial perfusion, Circulation 58 (3) (1978) 381–391.
[84] N. Westerhof, C. Boer, R.R. Lamberts, P. Sipkema, Cross-talk between cardiac muscle and coronary vasculature, Physiol. Rev. 86 (4) (2006) 1263–1308.
[85] A.G. Goodwill, G.M. Dick, A.M. Kiel, J.D. Tune, Regulation of coronary blood flow, Compr. Physiol. 7 (2) (2011) 321–382.
[86] G. Kassab, Coronary Circulation, Springer, 2019.
[87] L. Fan, Y. Sun, J.S. Choy, G.S. Kassab, L.C. Lee, Mechanism of exercise intolerance in heart diseases predicted by a computer model of myocardial demand-supply feedback system, Comput. Methods Programs Biomed. 227 (2022) 107188.
[88] J. Liu, B. Mao, Y. Feng, B. Li, J. Liu, Y. Liu, Closed-loop geometric multi-scale heart-coronary artery model for the numerical calculation of fractional flow reserve, Comput. Methods Programs Biomed. 208 (2021) 106266.
[89] X. Zuo, Z. Xu, H. Jia, Y. Mu, M. Zhang, M. Yuan, C. Wu, Co-simulation of hypertensive left ventricle based on computational fluid dynamics and a closed-loop network model, Comput. Methods Programs Biomed. 216 (2022) 106649.
[90] M. Toma, S. Singh-Gryzbon, E. Frankini, Z. Wei, A.P. Yoganathan, Clinical impact of computational heart valve models, Materials (Basel) 15 (9) (2022) 3302.

[91] A. Caiazzo, R. Guibert, I.E. Vignon-Clementel, A reduced-order modeling for efficient design study of artificial valve in enlarged ventricular outflow tracts, Comput. Methods Biomech. Biomed. Eng. 19 (12) (2016) 1314–1318.
[92] X. Shen, L. Bai, L. Cai, X. Cao, A geometric model for the human pulmonary valve in its fully open case, PLoS ONE 13 (6) (2018) e0199390.
[93] L. Feng, H. Gao, N. Qi, M. Danton, N.A. Hill, X. Luo, Fluid–structure interaction in a fully coupled three-dimensional mitral–atrium–pulmonary model, Biomech. Model. Mechanobiol. 20 (4) (2021) 1267–1295.
[94] Y.H. Loke, F. Capuano, E. Balaras, L.J. Olivieri, Computational modeling of right ventricular motion and intracardiac flow in repaired tetralogy of Fallot, Cardiovasc. Eng. Technol. 13 (1) (2022) 41–54.
[95] L. Asner, M. Hadjicharalambous, R. Chabiniok, D. Peressutti, E. Sammut, J. Wong, G. Carr-White, R. Razavi, A. King, N. Smith, et al., Patient-specific modeling for left ventricular mechanics using data-driven boundary energies, Comput. Methods Appl. Mech. Eng. 314 (2017) 269–295.
[96] M.R. Pfaller, J.M. Hörmann, M. Weigl, A. Nagler, R. Chabiniok, C. Bertoglio, W.A. Wall, The importance of the pericardium for cardiac biomechanics: from physiology to computational modeling, Biomech. Model. Mechanobiol. 18 (2019) 503–529.